Shape from Shading Under Various Imaging Conditions

Abdelrehim H. Ahmed and Aly A. Farag
Computer Vision and Image Processing Laboratory (CVIP)
University of Louisville, Louisville, KY, 40292
abdo,farag@cvip.uofl.edu

Abstract

Most of the shape from shading (SFS) algorithms have been developed under the simplifying assumptions of a Lambertian surface, an orthographic projection, and a distant light source. Due to the difficulty of the SFS problem, only a small number of algorithms have been proposed for surfaces with non-Lambertian reflectance, and among those, only very few algorithms are applicable for surfaces with specular and diffuse reflectance. In this paper we propose a unified framework that is capable of solving the SFS problem under various settings of imaging conditions i.e., Lambertian or non-Lambertian, orthographic or perspective projection, and distant or nearby light source. The proposed algorithm represents the image irradiance equation of each setting as an explicit Partial Differential Equation (PDE). In our implementation we use the Lax-Friedrichs sweeping method to solve this PDE. To demonstrate the efficiency of the proposed algorithm, several comparisons with the state of the art of the SFS literature are given.

1. Introduction

The Shape from shading (SFS) problem consists of recovering the 3D-shape of a scene through the analysis of the brightness variation in a single image. SFS was formally introduced in the original work of Horn [5] over 30 years ago. Since then, SFS became a well-known problem in computer vision. Horn formulated the SFS problem by a nonlinear first order partial differential equation (PDE) called the *image irradiance equation*. This equation models the relation between the shape of an object and its image brightness under known illumination conditions. In general, the brightness of a surface patch depends on its orientation relative to both the light source and the viewer. Under the simplifying assumption that the viewer and the light source are far from the object, the *image irradiance equation* can be written as follows:

$$E(\boldsymbol{x}) = R(\hat{\boldsymbol{n}}(\boldsymbol{x})) \tag{1}$$

where $E(\boldsymbol{x})$ is the image irradiance at the point $\boldsymbol{x}$ and $R(.)$ is the radiance of a surface patch with unit normal $\hat{\boldsymbol{n}}(\boldsymbol{x})$. For simplification purposes, most of the algorithms in SFS literature, e.g., [4, 17] assumed that the surface has a Lambertian reflectance, i.e., the surface reflects the light equally in all directions. In this case the reflectance map is the cosine of the angle between the unit vector $\hat{\boldsymbol{s}}$ in the light direction and the normal vector $\hat{\boldsymbol{n}}$:

$$E(\boldsymbol{x}) = R = cos\angle(\hat{\boldsymbol{s}}, \hat{\boldsymbol{n}}) = \hat{\boldsymbol{s}} \cdot \hat{\boldsymbol{n}} \tag{2}$$

which leads to the first PDE studied in the SFS literature:

$$I(\boldsymbol{x})\sqrt{1 + |\nabla u(\boldsymbol{x})|^2} + \hat{\boldsymbol{s}} \cdot (\nabla u(\boldsymbol{x}), -1) = 0. \tag{3}$$

where $u(\boldsymbol{x})$ is the surface height at point $\boldsymbol{x} = (x, y)$ above some reference plane. Note that the image irradiance E has been replaced by the measured image gray value I by assuming a linear relationship between them and dropping the scaling factor.

It is worth mentioning that Eq.(3) is not the most general equation of SFS, indeed, it is the simplest. Under real world circumstances the surface materials are not Lambertian, and in many cases the camera and the light are not far away from the object. For the sake of simplicity, Eq.(3) is the most studied model in the SFS literature and only a few reported studies have been concerned with more realistic modeling such as surfaces with non-Lambertian reflections [8, 16, 1] or perspective camera [14, 1].

The first attempt to solve the SFS problem under a general setting was studied by Horn [6]. In that work, Horn formulated the problem using a perspective camera, nearby light source, and an arbitrary reflectance and used the characteristic strip method to solve the resulted image irradiance equation. The main drawbacks of the characteristic strip method are accumulation of errors, noise sensitivity, and the uneven sampling of the image [3].

Lee and Kuo [8] presented a SFS algorithm for generalized reflectance map. They discretized the image irradiance equation with a triangular element surface model which involved only the depth variables. The shape was computed

1-4244-1180-7/07/$25.00 ©2007 IEEE

by linearizing the resulted nonlinear equations and minimizing a quadratic energy functional. In addition to being computationally expensive, the given results for this method were not promising. According to their modeling, Lee and Kuo noticed that "the non-Lambertian surface can hardly be recovered correctly with two photometric stereo images" [8].

SFS algorithms can be categorized into four main groups [23]: minimization approaches, propagation approaches, local approaches, and linear approaches. To solve the SFS problem under more comprehensive modeling conditions, we need very powerful mathematical tools. Basically, we can choose between the propagation approaches or energy minimization approaches since the applicability of the local approaches is limited, and the reasonability of the linear approximation of the reflectance map is questionable [3].

In this paper, we adopt the propagation approaches, to propose a unified framework for SFS that can handle different classes of imaging models for surface reflectance, camera projection, and light source location.

2. Reflectance models

This section gives a very brief description for the reflectance models that we consider in this work. In addition to the Lambertian model we have Oren-Nayar diffuse reflection model for rough surfaces [10], Wolff diffuse reflection model for smooth surfaces [21], and Ward model for surfaces with hybrid reflection [20].

The Oren-Nayar reflectance model [10] can be seen as a generalization of lambertian reflectance for rough diffuse surfaces. In that model the surface is composed of a collection of long symmetric V-cavities with two opposing facets for each cavity. The roughness of the surface is specified using a Gaussian distribution for the orientations of the facets. Using the geometry illustrated in Figure 1, a simplified expression for Oren-Nayar model is given by [10]:

$$L_r = \frac{\rho}{\pi} L_i \cos\theta_i (A + B \ \sin\alpha \tan\beta \max[0, \cos(\phi_r - \phi_i)]);$$
$$\text{where} \ \ A = 1 - 0.5\frac{\sigma^2}{\sigma^2 + 0.33} \ \ , B = 0.45\frac{\sigma^2}{\sigma^2 + 0.09} \ . \tag{4}$$

The parameter σ denotes the standard deviation of the Gaussian distribution, and it is used as a measure of the surface roughness, $\alpha = \max[\theta_r, \theta_i]$, $\beta = \min[\theta_r, \theta_i]$ and ρ is the diffuse albedo.

Wolff [21] developed a reflection model for smooth surfaces where the inhomogeneous dielectric material was modeled as a collection of scatterers contained in a uniform medium with index of refraction different from that of air. The diffuse reflected radiation results from refraction of incident light into the dielectric medium, producing multiple

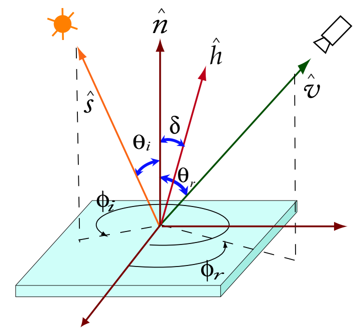

Figure 1. Definitions of reflection parameters and angles. $\hat{\boldsymbol{h}} = (h_x, h_y, h_z) = \frac{\hat{\boldsymbol{s}} + \hat{\boldsymbol{v}}}{|\hat{\boldsymbol{s}} + \hat{\boldsymbol{v}}|}$

internal scattering, followed by refraction back out into air. The reflected radiance of Wolff's model is expressed by:

$$\begin{aligned} L_r =& \varrho \ L_i \cos\theta_i \times [1 - F(\theta_i, n)] \\ & \times [1 - F(\sin^{-1}(\sin\theta_r/n), 1/n)] \end{aligned} \tag{5}$$

Where ϱ is the total diffuse albedo and the terms $F(.,.)$ refer to the Fresnel reflection function [2].

Wolff et al. [22] suggested to incorporate the reflectance model of Wolff in the Oren-Nayar model to get a general diffuse reflectance model (we call it Oren-Nayar-Wolff model) that works for smooth and rough surfaces. They suggested to replace the 'A' term in Oren-Nayar model (Eq. 4) by:

$$\begin{aligned} & [1 - 0.5\sigma^2/(\sigma^2 + 0.33)] \times [1 - F(\theta_i, n)] \\ & \times [1 - F(\sin^{-1}(\sin\theta_r/n), 1/n)] \end{aligned} \tag{6}$$

Unlike the previous models which model the diffuse reflection only, the reflectance model proposed by Ward [20] accounts for both the diffuse and the specular components of the reflection. Ward's model is physically realizable variant of Phong model [12] and it has a simple formula that is constrained to obey fundamental physical laws, such as conservation of energy and reciprocity. The model has been validated experimentally by many measurements from real samples collected by a simple reflectometry device [20]. The expression for Ward's reflectance model is given by:

$$L_r = \frac{\rho_d \ \cos\theta_i}{\pi} + \rho_s \sqrt{\frac{\cos\theta_i}{\cos\theta_r}} \ \frac{\exp[-\tan^2\delta/\sigma^2]}{4 \ \pi \ \sigma^2}; \tag{7}$$

where ρ_d and ρ_s are the diffuse and specular reflectance albedos, σ is the standard deviation of the surface roughness and δ is the angle between vectors $\hat{n}$ and $\hat{h}$ as illustrated in Fig. 1 .

Figure 2 shows four synthetic images of a sphere generated with Lambertian, Oren-Nayar, Wolff and Ward models. The sphere is illuminated from the direction $(0, 0, 1)$ and

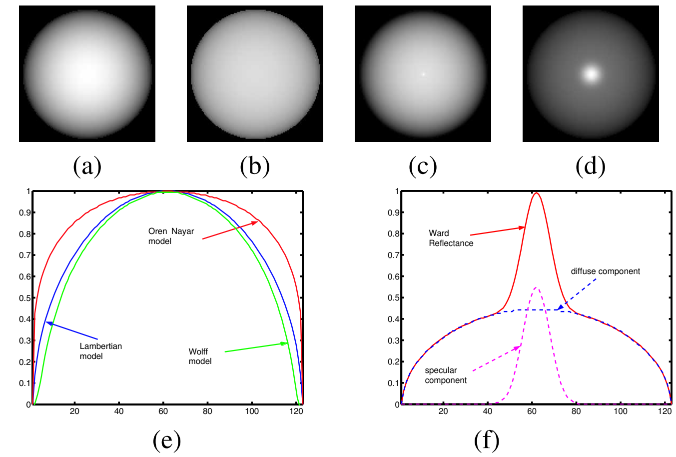

Figure 2. The appearance of a synthetic sphere under: (a) Lambertian, (b) Oren-Nayar, (c) Wolff, and (d) Ward reflectance models. (e) cross section of the brightness of the images: a,b, and c. (f) cross section of image (d) and the two components of Ward model.

viewed also from the direction $(0, 0, 1)$. In the Oren-Nayar model, the reflection across a rough surface is brighter than what is predicted by Lambert's law, which gives the rough surfaces a flatter appearance. On the other hand, the brightness of the smooth surfaces as modeled by Wolff's reflectance is darker than the prediction of Lambert's model, especially at large angles of reflection and/or large angles of incidence, see Fig. 2(e).

The two components of the Ward reflectance model are plotted in Fig. 2(f). The diffuse component is just a Lambertian reflection and it depends only on the value of the incident angle, while the specular component depends on the relative ordination of the surface with respect to both the illumination and viewing directions. As it is clear from Fig. 2(d,f), the specular component is insignificant everywhere except around the center of the sphere where the value of the angle δ becomes close to zero.

3. Unified framework for SFS problem

In this paper we present a unified approach, which can solve several classes of imaging conditions. For each model, we derive the image irradiance equation and formulate it as a Hamilton-Jacobi partial differential equation (PDE) with Dirichlet boundary conditions. Since solving the image irradiance equation is difficult especially under comprehensive image modeling, a powerful numerical tool is needed. One of the candidate tools is the Lax-Friedrichs Sweeping (LFS) method. The LFS method was presented by Kao et al. [7] where a fast sweeping method based on Lax-Friedrichs Hamiltonian was designed to approximate the viscosity solutions of static Hamilton-Jacobi equations. The main advantage of LFS is its ability to deal with both convex and non-convex Hamiltonians with any degree of complexity.

	camera	light source	reflectance	literature
A	orthographic	at infinity	Lambertian	[4, 11, 18]
B	orthographic	at infinity	Oren-Nayar	[18, 16]
C	orthographic	at infinity	Oren-Nayar-Wolff	[16]
D	orthographic	at infinity	Ward	*new*
E	perspective	at the camera o.c.	Lambertian	[9, 13]
F	perspective	at the camera o.c.	Oren-Nayar	[1]
G	perspective	at the camera o.c.	Oren-Nayar-Wolff	*new*

Table 1.

Recently LFS has been used in the SFS literature [1] to solve the SFS problem for a class of non-Lambertian diffuse surfaces. In this paper we build on the work of Ahmed and Farag [1] and generalize their approach for various image conditions.

Table 1 gives a list for several combinations of imaging conditions. Due to space limitation, we describe the proposed approach for four models: Model 'A', 'B', 'D', and 'G'.

For each modeling condition the proposed approach processes as follows:

- derive the image irradiance equation as a PDE
- put the PDE in the following form:

$$\begin{cases} H(\nabla u, \boldsymbol{x}) = R(\boldsymbol{x}) & \forall \boldsymbol{x} \in \Omega \\ u(\boldsymbol{x}) = \psi(\boldsymbol{x}) & \forall \boldsymbol{x} \in \partial\Omega, \end{cases} \tag{8}$$

  Where ψ is a Dirichlet boundary condition. In this paper, we assume that the object is in front of a background that is used as a boundary condition with zero depth.

- use the previous form and apply the LFS method [7, 1] on the input image to recover the shape of the scene.

3.1. Symbols and Notations

This section is dedicated to clarify the symbols and notations that are used in the following sections. The compact domain $\Omega \subset \mathbb{R}^2$ is the image domain and $I : \Omega \rightarrow [0, 1]$ is the image intensity.

When the camera has an orthographic projection the surface is represented by $\mathcal{S} = \{(\boldsymbol{x}, u(\boldsymbol{x})) \quad / \boldsymbol{x} \in \Omega\}$. For perspective projection, we use the same representation as in [15] where the surface is represented by $\mathcal{S} = \{\frac{f\ u(\boldsymbol{x})}{\sqrt{|\boldsymbol{x}|^2+f^2}}(\boldsymbol{x}, -f) \quad / \boldsymbol{x} \in \Omega\}$ with f denotes the focal length of the camera, see Fig. (3).

The unit vectors $\hat{\boldsymbol{s}} = (s_x, s_y, s_z)$ and $\hat{\boldsymbol{v}} = (v_x, v_y, v_z)$ are used to specify the directions of the light and the camera respectively. The symbol $\boldsymbol{\tau_s}$ refers to the first two components of $\hat{\boldsymbol{s}}$. Similarly the symbol $\boldsymbol{\tau_v}$ refers to the first two components of $\hat{\boldsymbol{v}}$.

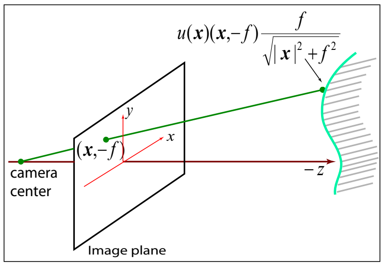

Figure 3. Modeling the camera by perspective projection.

3.2. Model 'A'

The simplest imaging model is obtained if the camera performs an orthographic projection of a surface that has Lambertian reflectance and illuminated by a point light source located far away from the surface. The image irradiance equation is obtained directly as explained in the introduction section:

$$I(\boldsymbol{x})\sqrt{1+|\nabla u(\boldsymbol{x})|^2}+\boldsymbol{\tau_s}\cdot\nabla u(\boldsymbol{x})-s_z=0,\ \forall\boldsymbol{x}\in\Omega \tag{9}$$

When the surface is illuminated by frontal light source at infinity, i.e., $\hat{\boldsymbol{s}}=(0,0,1)$, the last equation can be reduced to the *Eikonal equation*:

$$|\nabla u|-\sqrt{1/I(\boldsymbol{x})^2-1}=0. \quad \forall\boldsymbol{x}\in\Omega \tag{10}$$

This model is the most studied model in the SFS literature, e.g., [4, 11, 17, 19].

3.3. Model 'B'

By keeping the assumptions of orthographic projection and far light source, the previous model can be enhanced by utilizing a more general reflectance model such as Oren-Nayar model defined by Eq. 4.

This model has been studied by Samaras and Metaxas [18] where they used the Deformable Models to propose a technique for SFS and light direction estimation.

Also Ragheb and Hancock [16] solved the SFS problem under this modeling. Their method extracted the Lambertian component from non-Lambertian surfaces and then applied the Frankot and Chellappa's algorithm [4] to recover the shape.

From the geometry illustrated in Fig. 1 , and after some algebraic manipulations the image irradiance can be written as:

$$\begin{aligned}&I(x)\sqrt{1+|\nabla u|^2}-A(-\boldsymbol{\tau_s}\cdot\nabla u+s_z)\\&-B\min\left[1,\frac{-\boldsymbol{\tau_s}\cdot\nabla u+s_z}{-\boldsymbol{\tau_v}\cdot\nabla u+v_z}\right]\frac{g_s(\nabla u)g_v(\nabla u)(\hat{\boldsymbol{\tau}}_s\cdot\hat{\boldsymbol{\tau}}_v)}{\sqrt{1+|\nabla u|^2}}=0.\end{aligned} \tag{11}$$

where $g_s(\nabla u)=\sqrt{(1+|\nabla u|^2)-(-\boldsymbol{\tau_s}\cdot\nabla u+s_z)^2}$ and $g_v(\nabla u)=\sqrt{(1+|\nabla u|^2)-(-\boldsymbol{\tau_v}\cdot\nabla u+v_z)^2}$.

The expression of the Hamiltonian H is:

$$\begin{aligned}H&=I(x)\sqrt{1+|\nabla u|^2}-A\,(-\boldsymbol{\tau_s}\cdot\nabla u)\\&-B\ \min\left[1,\frac{-\boldsymbol{\tau_s}\cdot\nabla u+s_z}{-\boldsymbol{\tau_v}\cdot\nabla u+v_z}\right]\frac{g_s(\nabla u)\ g_v(\nabla u)\ (\hat{\boldsymbol{\tau}}_s\cdot\hat{\boldsymbol{\tau}}_v)}{\sqrt{1+|\nabla u|^2}}.\end{aligned}$$

and $R=A\ s_z$.

3.4. Model 'D'

In this model we assume that the surface has a hybrid reflection defined by Ward's model Eq. 7. The camera is assumed to have an orthographic projection and the light is located at infinity. From the geometry illustrated in Fig. 1, we derive the following expression for the irradiance equation:

$$\begin{aligned}&I(x)\left[\frac{\sqrt{1+|\nabla u|^2}}{-\boldsymbol{\tau_s}\cdot\nabla u+s_z}\right]-\frac{\rho_d}{\pi}\\&-\frac{\rho_s}{4\,\pi\sigma^2}\sqrt{\frac{1+|\nabla u|^2}{(-\boldsymbol{\tau_s}\cdot\nabla u+s_z)(-\boldsymbol{\tau_v}\cdot\nabla u+v_z)}}\\&\times\exp\left[\frac{-1}{\sigma^2}\frac{(1+|\nabla u|^2)-(-\hat{\boldsymbol{\tau}}_h\cdot\nabla u+h_z)^2}{(-\hat{\boldsymbol{\tau}}_h\cdot\nabla u+h_z)^2}\right]=0.\end{aligned} \tag{12}$$

The expressions of H and R are given by:

$$\begin{aligned}H&=I(x)\left[\frac{\sqrt{1+|\nabla u|^2}}{-\boldsymbol{\tau_s}\cdot\nabla u+s_z}\right]\\&-\frac{\rho_s}{4\,\pi\sigma^2}\sqrt{\frac{1+|\nabla u|^2}{(-\boldsymbol{\tau_s}\cdot\nabla u+s_z)(-\boldsymbol{\tau_v}\cdot\nabla u+v_z)}}\\&\times\exp\left[\frac{-1}{\sigma^2}\frac{(1+|\nabla u|^2)-(-\hat{\boldsymbol{\tau}}_h\cdot\nabla u+h_z)^2}{(-\hat{\boldsymbol{\tau}}_h\cdot\nabla u+h_z)^2}\right];\\R&=\frac{\rho_d}{\pi}.\end{aligned} \tag{13}$$

3.5. Model 'G'

In this model we use the Oren-Nayar-Wolff model for the surface reflectance. The camera has a perspective projection and the light source is assumed to be located at the optical center of the camera. Furthermore, we take into account the attenuation term $(1/r^2)$ of the illumination due to the distance between the light source and the surface.

Since the location of the light source is at the optical center of the camera, we have $\theta_i=\theta_r=\alpha=\beta\doteq\theta$ and the two Fresnel terms are equal to each other, therefore the expression of the image I under Oren-Nayar-Wolff model can be simplified to:

$$I(\boldsymbol{x})=\frac{A\ (1-F(\theta,n))^2\cos\theta+B\sin^2\theta}{r^2} \tag{14}$$

It is worth mentioning that Eq. 14 without the $(1/r^2)$ term was also obtained in [16] but under different assumptions.

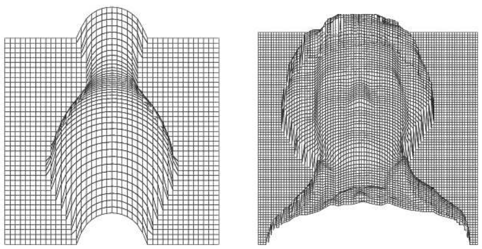

Figure 4. Ground truth maps used to generate the synthetic images.

In[16] the camera has an orthographic projection and the light source is far away from the object, furthermore, the light direction and the camera direction are assumed to be equal to each other.

After some algebraic manipulations and using the change of variable $w = ln(u)$, we get the following irradiance equation:

$$-e^{-2w} + I(\boldsymbol{x})f^2 \times \frac{Q(\nabla w, \boldsymbol{x}) + 1}{A\ (1 - F(\theta, n))^2\ \sqrt{Q(\nabla w, \boldsymbol{x}) + 1} + B\ Q(\nabla w, \boldsymbol{x})} = 0. \quad (15)$$

where,

$$Q(\nabla w, \boldsymbol{x}) = (f^2|\nabla w|^2 + (\nabla w \cdot \boldsymbol{x})^2) \times (|\boldsymbol{x}|^2 + f^2)/f^2$$

and the Fresnel function is approximated by [22]:

$$F(\theta, n) = 0.935\left[(2\theta/\pi)^5 + 0.07\right].$$

The associated expressions for H and R are:

$$H = I(\boldsymbol{x})f^2 \frac{Q(\nabla w, \boldsymbol{x}) + 1}{A\ (1 - F(\theta, n))^2\ \sqrt{Q(\nabla w, \boldsymbol{x}) + 1} + B\ Q(\nabla w, \boldsymbol{x})};$$
$$R = \varepsilon > 0\ . \quad (16)$$

4. Experimental results and discussion

The performance of the proposed approach is evaluated using both synthetic and real images. The synthetic images were generated using the depth map of two objects, a synthetic vase and Mozart face as shown on Fig. 4. The maximum depth of the vase is 36.55, while the maximum depth is 85.15 for Mozart. For real data, the test set consists of four real images shown on Fig. 9.

4.1. Synthetic images

In order to quantitatively analyze the performance of the proposed SFS, we follow the same evaluation methodology, described in the survey paper by Zhang et al. [23]. The following error measures are used:

Mean and standard deviation of the error: For each synthetic image, we compare the recovered depth with the reference depth map and compute the mean and the standard deviation of the absolute error (after normalizing the output according to reference data).

Mean gradient error: This indicates the error in the surface orientation. We provide the mean of the absolute error in the two gradient components ($\partial u/\partial x$ and $\partial u/\partial y$). The gradient components are computed using the forward difference approximation.

4.1.1 Model 'A'

Figure 5 shows four synthetic images and their corresponding shapes recovered by the proposed SFS. The four synthetic images are generated using Model 'A'; two images are generated with $s = (0, 0, 1)$ while the other two images are generated with $s = (1, 0, 1)$.

To demonstrate the accuracy of our results, we compare the recovered shape of each test image with the result given in [18] for the same image. Also we report the best result obtained from the algorithms tested in [23]. The error measures are listed in Tables 2 and 3.

As can be clearly seen from the Fig. 5(b, d), and the error measures in Tables 2 and 3, the vase shape is recovered with very high precision for both cases. For the Mozart results, the recovered shape is quite good for the case of $s = (0, 0, 1)$ as shown on Fig 5(f), however, the result is less accurate for the case of $s = (1, 0, 1)$.

For all cases, except Mozart with $s = (1, 0, 1)$, the results of the proposed approach are better than the results of the algorithms reviewed in [23], and the algorithm in [18]. The degradation of the performance for the case of Mozart with $s = (1, 0, 1)$ is due to a lack of brightness information in the left side of Mozart face, see Fig 5(g). Since the proposed approach is a propagation approach, its performance is greatly affected by this missing information.

4.1.2 Models 'B', 'D', and 'G'

The synthetic images and the results of the proposed approach for Models 'B', 'D', and 'G' are shown on Fig. 6, Fig. 7, and Fig. 8 respectively.

Unlike Model 'A', there is no benchmarks available for SFS under the rest of the proposed modeling conditions. Therefore, we report the values of the error measures in Table 4 and we use their corresponding numbers in Table 2 as indicators for the accuracy of the results.

The results for all models illustrate that the shape of the vase is successfully reconstructed with a high accuracy and the error is very limited as indicated by the error measures in Table 4. Similarly, the recovered shape of Mozart under Model 'G', shown on Fig 8, is very promising.

Even though the recovered shapes of Mozart using the proposed approach for Model 'B' and 'D' have lower accuracy than the recovered shape under Model 'G', the error

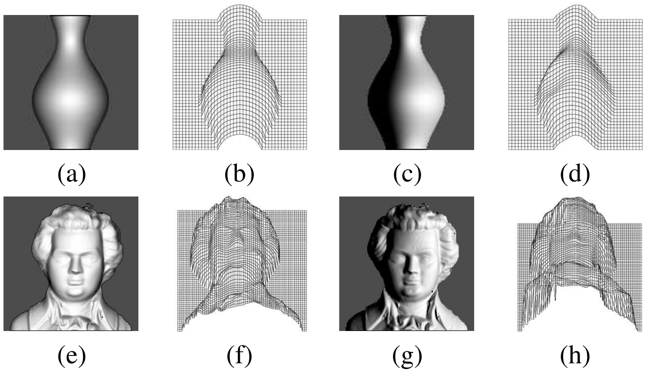

Figure 5. Experiments on two synthetic images for the vase and two for Mozart: (a,e) are generated using model 'A' with $s = (0, 0, 1)$ and their recovered shapes are displayed in (b,f) respectively. (c,g) are generated with $s = (1, 0, 1)$ and their recovered shapes are displayed in (d,h) respectively.

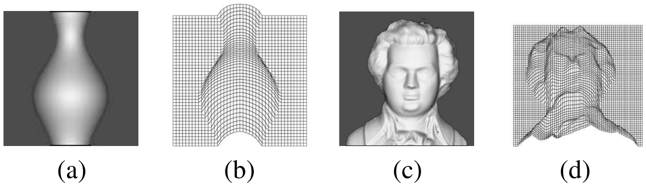

Figure 6. Experiments on two synthetic images for the vase and Mozart: (a,c) are generated using model 'B' with $s = (0, 0, 1)$, $v = (0, 0, 1)$ and $\sigma = 0.2$ rad. The recovered shapes are displayed in (b,d).

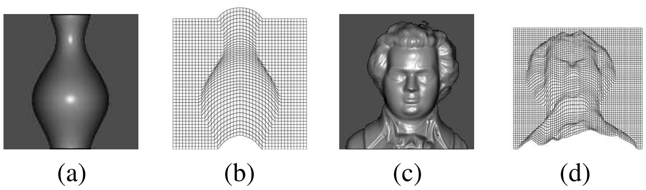

Figure 7. Experiments on two synthetic images for the vase and Mozart: (a,c) are generated using model 'D' with $s = (0, 0, 1)$, $v = (0, 0, 1)$, $\sigma = 0.2$ rad, $\rho_d = 0.67$ and $\rho_s = 0.075$;. The recovered shapes are displayed in (b,d).

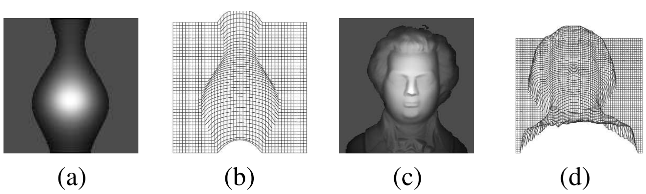

Figure 8. Experiments on two synthetic images for the vase and Mozart: (a,c) are generated using model 'G' with $\sigma = 0.5$ rad. The recovered shapes are displayed in (b,d).

measures are still comparable to their corresponding numbers in Table 2.

	methods	Vase	Mozart
mean of the absolute error	Best [23]	8.1	15.1
	[18]	2.8	8.1
	proposed	0.22	4.0
standard deviation of the absolute error	Best [23]	11.1	18.2
	[18]	2.0	6.3
	proposed	0.4	5.3
mean of the gradient error	Best [23]	1.2	1.3
	[18]	0.2	0.5
	proposed	0.05	0.3

Table 2. The error measures for the three SFS algorithms under Model 'A' with $s = (0, 0, 1)$.

	methods	Vase	Mozart
mean of the absolute error	Best [23]	7.9	7.7
	[18]	4.1	4.2
	proposed	1.2	6.6
standard deviation of the absolute error	Best [23]	13.9	14.6
	[18]	2.6	3.4
	proposed	2.2	10.9
mean of the gradient error	Best [23]	0.9	0.6
	[18]	0.5	0.3
	proposed	0.1	0.6

Table 3. The error measures for the three SFS algorithms under Model 'A' with $s = (1, 0, 1)$.

	Model	Vase	Mozart
mean of the absolute error	'B'	0.6	10
	'D'	0.8	10.4
	'G'	0.4	4.2
standard deviation of the absolute error	'B'	1.0	13.2
	'D'	1.3	13.0
	'G'	1.2	5.7
mean of the gradient error	'B'	0.08	0.51
	'D'	0.09	0.53
	'G'	0.07	0.49

Table 4. The error measures for the three SFS algorithms under Models 'B', 'D', and 'G'.

4.2. Real images

In order to demonstrate the applicability of the proposed SFS approach for real data, we have conducted experiments on four real images; a rabbit, a real vase, a face, and a hair dryer. These images and their recovered shapes are shown on Fig. 9. For each image, we manually selected the model that best fits the imaging conditions, i.e., the surface material, and the locations of the camera and the light source relative to the object. As shown on Fig. 9, the results are relatively very accurate even for the face which has many details.

4.3. Timing

Table 5 reports the execution time of the proposed algorithm for all the experiments that are given in section 4.1 and 4.2. The CPU timing is computed on a PC workstation with Pentium4 3.00GHz processor and 2 GB RAM. For all the experiments the execution time is less than 14 second, which indicates the efficiency of the numerical algorithm for both synthetic and real images under various imaging conditions.

In order to investigate the convergence of the numerical

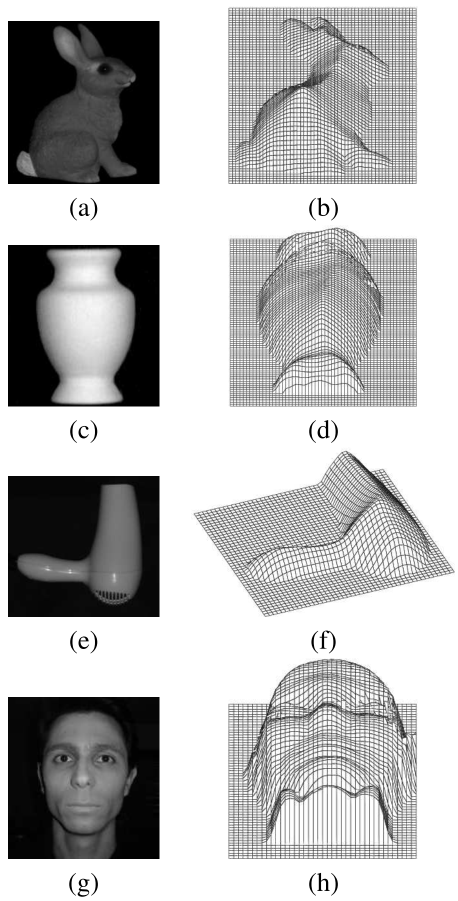

Figure 9. Experiments on four real images. (a,b) a rabbit and its recovered shape using Model 'A'. (c,d) a vase and its recovered shape using Model 'B'. (e,f) a hair dryer and its recovered shape using Model 'D'. (g,h) a face (courtesy of [14]) and its recovered shape using Model 'G'.

image name	image size	model	CPU time in sec
synthetic vase	128×128	'A'	0.5
synthetic vase	128×128	'B'	1.5
synthetic vase	128×128	'D'	1.8
synthetic vase	128×128	'G'	0.3
synthetic Mozart	256×256	'A'	2
synthetic Mozart	256×256	'B'	6
synthetic Mozart	256×256	'D'	13
synthetic Mozart	256×256	'G'	5
rabbit	292×224	'A'	8
real vase	241×173	'B'	3
hair dryer	190×204	'D'	5
face	205×154	'G'	2

Table 5. The CPU timing.

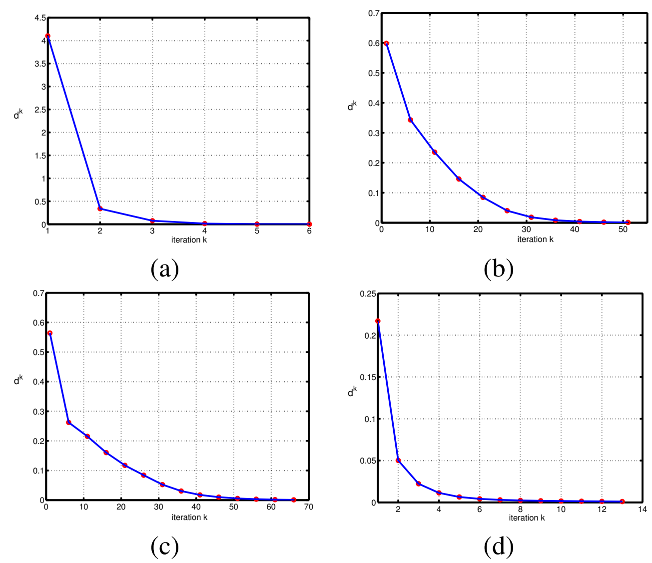

Figure 10. The difference between two consecutive approximations: $d^k = \sum_{i=1}^{M} \sum_{j=1}^{N} |U_{i,j}^k - U_{i,j}^{k-1}|/(M \times N)$ for the synthetic vase results with (a) Model 'A', (b) Model 'B', (c) Model 'D', (d) Model 'G'.

algorithm, the values of the difference between two consecutive approximations are provided. These values are computed as follows:

$$d^k = \frac{\sum_{i=1}^{M} \sum_{j=1}^{N} |U_{i,j}^k - U_{i,j}^{k-1}|}{M \times N} \quad (17)$$

where $U_{i,j}^k$ is the approximation of $u(\boldsymbol{x})$ at step k, $U_{i,j}^{k-1}$ is the approximation at step $k-1$, and $M \times N$ is the image size.

The values of d^k are computed for the synthetic vase experiment in section 4.1. Figure 10 displays the values of d^k on the y-axis and the number of iterations k on the x-axis. As it is shown on the figure, the algorithm converges to the solution in very few iterations for the Model 'A' and 'G', while it takes more iterations for Model 'B' and Model 'D'.

5. Conclusion

In this paper we have formulated the SFS with four different imaging models. The first two models are for diffuse surfaces under orthographic projection, the third model is for hybrid surfaces under orthographic projection, and the last model is for diffuse surfaces under perspective projection. Formulating the SFS problem using realistic assumptions can lead to better estimation of the scene shape, meanwhile it makes solving the SFS much harder. For the four models, the image irradiance equations are derived and the resulted PDE's are solved using a fast numerical algorithm based on Lax-Friedrichs sweeping method. The main advantage of this numerical algorithm is its capability of handling the complexity of the different PDE's. The proposed approach is evaluated using both synthetic and real data sets and the experimental results show the potential of the approach.

6. Acknowledgements

This research has been supported by National Science Foundation (NSF) (Grant IIS-0513974)

References

[1] A. H. Ahmed and A. A. Farag. A new formulation for shape from shading for non-lambertian surfaces. In *International Conference on Computer Vision and Pattern Recognition CVPR06*, pages 1817–1824, NY, USA, 2006.

[2] M. Born and E. Wolf. *Principle of Optics*. Pergamon, New York, 1970.

[3] J.-D. Durou, M. Falcone, and M. Sagona. A survey of numerical methods for shape from shading. 2004-2-r, Institut de Recherche en Informatique de Toulouse (IRIT), 2004.

[4] R. Frankot and R. Chellappa. A method for enforcing integrability in shape from shading algorithms. *IEEE Trans. on Pattern Analysis and Machine Intelligence*, 10(4):439–451, 1988.

[5] B. Horn. *Shape from Shading: A Method for Obtaining the Shape of a Smooth Opaque Object from One View*. PhD thesis, Massachusetts Inst. of Technology, Cambridge, Massachusetts, 1970.

[6] B. Horn. Obtaining shape from shading information. In P. H. Winston, editor, *The Psychology of Computer Vision*, chapter 4, pages 115–155. McGraw-Hill, New York, 1975.

[7] C. Y. Kao, S. Osher, and J. Qian. Lax-friedrichs sweeping scheme for static hamilton-jacobi equations. *Journal of Computational Physics*, 196(1):367 – 391, 2004.

[8] K. M. Lee and C.-C. J. Kuo. Shape from shading with a generalized reflectance map model. *Comput. Vis. Image Underst.*, 67(2):143–160, 1997.

[9] T. Okatani and K. Deguchi. Shape reconstruction from an endoscope image by shape from shading techniques for a point light source at the projection center. *Computer Vision and Image Understanding*, 66(2):119–131, 1997.

[10] M. Oren and S. Nayar. Generalization of the lambertian model and implications for machine vision. *International Journal of Computer Vision*, 14(3):227 – 251, 1995.

[11] A. Pentland. Local shading analysis. *IEEE Trans. on Pattern Analysis and Machine Intelligence*, 6(2):170–187, 1984.

[12] B. T. Phong. Illumination for computer generated pictures. *Commun. ACM*, 18(6):311–317, 1975.

[13] E. Prados and O. Faugeras. Unifying approaches and removing unrealistic assumptions in shape from shading: Mathematics can help. In *European Conference on Computer Vision ECCV04*, Prague,Czech Republic, May 2004.

[14] E. Prados and O. Faugeras. Shape from shading: a well-posed problem? In *International Conference on Computer Vision and Pattern Recognition CVPR05*, San Diego, CA, USA, June 2005.

[15] E. Prados, O. Faugeras, and F. Camilli. Shape from shading: a well-posed problem ? RR 5297, INRIA Research, Aug. 2004.

[16] H. Ragheb and E. Hancock. Surface normals and height from non-lambertian image data. In *Second International Symposium on 3D Data Processing, Visualization and Transmission (3DPVT'04)*, Greece, 2004.

[17] E. Rouy and A. Tourin. A viscosity solutions approach to shape from shading. *SIAM J. Numerical Analysis*, 29(3):867–884, 1992.

[18] D. Samaras and D. Metaxas. Incorporating illumination constraints in deformable models for shape from shading and light direction estimation. *IEEE Trans. Pattern Anal. Mach. Intell.*, 25(2):247–264, 2003.

[19] P. Tsai and M. Shah. Shape from shading using linear approximation. *Image and Vision Computing J.*, 12(8):487–498, 1994.

[20] G. J. Ward. Measuring and modeling anisotropic reflection. In *Proceedings of the 19th annual conference on Computer graphics and interactive techniques,SIGGRAPH'92*, pages 265–272, 1992.

[21] L. B. Wolff. Diffuse reflection. In *International Conference on Computer Vision and Pattern Recognition CVPR92*, page 472478, Urbana-Champaign Illinois, 1992.

[22] L. B. Wolff, S. K. Nayar, and M. Oren. Improved diffuse reflection models for computer vision. *Int. J. Comput. Vision*, 30(1):55–71, 1998.

[23] R. Zhang, P.-S. Tsai, J.-E. Cryer, and M. Shah. Shape from shading: A survey. *IEEE Trans. on Pattern Analysis and Machine Intelligence*, 21(8):690–706, 1999.